

Article

Single Step Process for Crystalline Ni-B Compounds

Mahboobeh Shahbazi, Henrietta Cathey, Natalia Danilova and Ian D.R. Mackinnon * 

Institute for Future Environments and Science and Engineering Faculty, Queensland University of Technology (QUT), Brisbane QLD 4001, Australia; mahboobeh.shahbazi@qut.edu.au (M.S.); henrietta.cathey@qut.edu.au (H.C.); natalia.danilova@qut.edu.au (N.D.)

* Correspondence: ian.mackinnon@qut.edu.au; Tel.: +61-7-3138-7656

Received: 8 June 2018; Accepted: 20 July 2018; Published: 22 July 2018



Abstract: Crystalline Ni₂B, Ni₃B, and Ni₄B₃ are synthesized by a single-step method using autogenous pressure from the reaction of NaBH₄ and Ni precursors. The effect of reaction temperature, pressure, time, and starting materials on the composition of synthesized products, particle morphologies, and magnetic properties is demonstrated. High yields of Ni₂B (>98%) are achieved at 2.3–3.4 MPa and ~670 °C over five hours. Crystalline Ni₃B or Ni₄B₃ form in conjunction with Ni₂B at higher temperature or higher autogenous pressure in proportions influenced by the ratios of initial reactants. For the same starting ratios of reactants, a longer reaction time or higher pressure shifts equilibria to lower yields of Ni₂B. Using this approach, yields of ~88% Ni₄B₃ (single phase orthorhombic) and ~72% Ni₃B are obtained for conditions 1.9 MPa < P_{max} < 4.9 MPa and 670 °C < T_{max} < 725 °C. Gas-solid reaction is the dominant transformation mechanism that results in formation of Ni₂B at lower temperatures than conventional solid-state methods.

Keywords: nickel boride synthesis; sodium borohydride; microprobe analysis; microstructure; autogenous pressure

1. Introduction

Nickel boride compounds are useful industrial materials due to their microhardness, high chemical and thermal stability, excellent selectivity and activity for liquid phase reactions and their effectiveness as catalysts. The Ni-B system comprises several stable crystalline compounds for which their structures are well described in the literature: NiB, Ni₃B, Ni₂B, Ni₄B₃, Ni₇B₃, and Ni₂₃B₆ [1–6]. Examples of the three most common forms, orthorhombic Ni₄B₃, Ni₂B, and Ni₃B, are shown in Figure 1. Boron-rich nickel borides are paramagnetic while nickel-rich boride compounds are soft ferromagnets [3,7–10].

The functionality of Ni-B compounds is dependent on the form—amorphous or crystalline—often determined by the method of synthesis. For example, amorphous Ni-B compounds are highly active catalysts for hydrogenation and other organic reactions and are prepared by chemical reduction [11,12] using hydrolysis of NaBH₄ with a metal salt [13,14]. Crystalline forms of Ni-B are determined by sintering temperatures and heating duration applied to a precursor material which may include amorphous Ni-B compositions [15]. A good example of functional dependence is recently described by Jiang et al. [4] who developed an efficient oxygen evolution reaction (OER) electrocatalyst using Ni₃B nanoparticle cores surrounded by nickel borate shells [16]. In their work, the crystallinity of Ni₃B shells is found to affect the OER electrocatalyst activity. Partially crystalline Ni₃B shells exhibit a higher OER activity than the amorphous or fully crystalline counterparts [13].

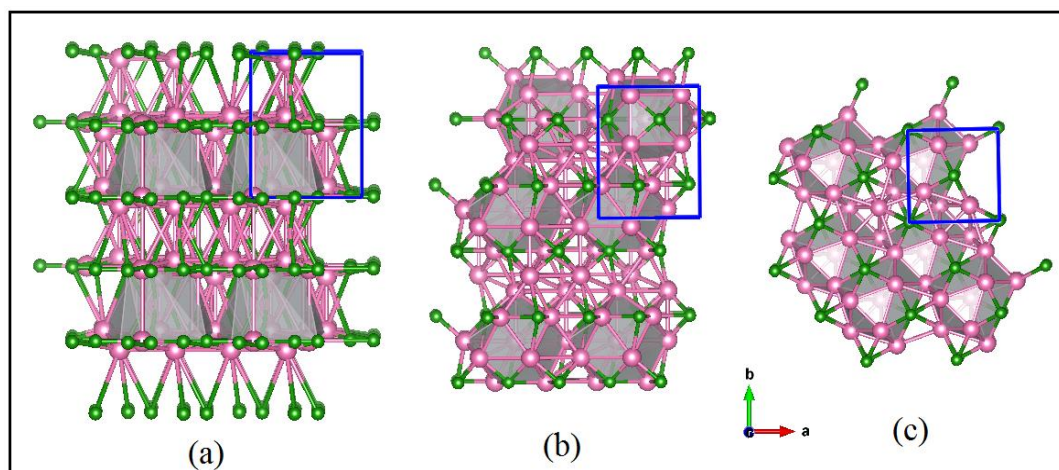


Figure 1. Crystal structures of (a) Orthorhombic Ni_4B_3 , (b) Ni_3B and (c) Ni_2B . Unit cells are outlined in blue. Ni atoms are pink and B atoms are green.

Solid state synthesis of boron compounds is usually undertaken at high temperature due to the high melting point of boron. For example, Ni_3B is synthesized at $1000\text{ }^\circ\text{C}$ [4], Ni_2B at $1200\text{ }^\circ\text{C}$ [17] and Ni_4B_3 at $750\text{--}900\text{ }^\circ\text{C}$ [5]. Several other lower temperature methods have been suggested for synthesis of nickel boride compounds including ball milling of the elements [18], boronizing of pure nickel [19], and a solvo-thermal route [20]. Schlesinger et al. [21] reported a simple synthesis of nickel boride using nickel salts and sodium borohydride, which results in the formation of a black precipitate with elemental ratios equivalent to Ni_2B . Their work focused on NaBH_4 hydrolysis with Co and the effectiveness of the product as an accelerator for the production of organic acids. As a result, structural data on the form of the black precipitate with Ni_2B composition are not available [21].

The room temperature synthesis of a Ni-B compound via hydrolysis of metal borohydrides is also reported by Caputo et al. [15]. In both cases, the amorphous Ni-B precipitate requires sintering at $>250\text{ }^\circ\text{C}$ in ultrahigh purity argon for a minimum of 2 h to achieve a crystalline form [12,22,23]. Nanoparticles of nickel diboride (NiB_2) have also been produced by reducing nickel iodide with lithium borohydride in anhydrous oxygen-free tetrahydrofuran (THF) [24].

In this article, we report the fabrication of Ni_2B , Ni_3B , and orthorhombic Ni_4B_3 (o- Ni_4B_3) compounds at moderate temperature and autogenous pressure using a Parr reactor. These syntheses utilize autogenous pressure derived from the decomposition of sodium borohydride in the presence of Ni. The optimum pressure attained via this process for Ni_2B synthesis is $\sim 2.3\text{--}3.4\text{ MPa}$ at a maximum temperature of $\sim 670\text{ }^\circ\text{C}$. We describe the structure and microstructure of these compounds using X-ray diffraction and electron beam methods. The influence of reaction temperature, pressure time and starting materials on the composition of synthesized products, particle morphologies, and magnetic properties is demonstrated.

2. Materials and Methods

2.1. Boride Synthesis

Molar ratios of Ni ($<150\text{ }\mu\text{m}$; 99.9% purity) and NaBH_4 powder (99.99% purity) supplied by Sigma-Aldrich (St. Louis, MO, USA) are weighed, gently ground in an agate mortar, and placed into a 50 mL Parr reactor within a controlled atmosphere glove box containing Argon (99.99% purity). Mixing of starting materials noted above does not approximate the well-known effects of ball-milling [18]. For some experiments, a boron nitride sleeve is introduced into the reactor to minimize reaction with Ni-rich side-walls of the reactor. Details of operational practices using this type of reactor are provided in earlier work [25,26].

The reactor design results in a thermal gradient of ± 200 °C between the bottom and top of the reactor during ramp up to the equilibration temperature. An advantage of this reactor design is that gaseous phases such as sodium and sodium hydride condense at the cooler top of the reactor. On cooling the reaction chamber to room temperature, the reactor is opened in the argon-filled glove box *via* slow pressure equilibration using a gas release valve.

Since all starting materials are placed at the base of the reactor and heating elements are located at the base, we have calibrated the actual temperature at different measured heights with the thermocouple readings, which are made at the center of the reactor. Calibrations show that the relative error in temperature estimates at the reactor base is ± 20 °C at ~ 400 °C. In this study, we use the calibrated temperatures for the base of the reactor. A consistent heating rate of 10 °C/min is used in all reactions, albeit at different temperatures, and the heating rate is held constant for varying periods of time. In general, the reactor heating rate is held constant to achieve temperatures at the reactor base of: (i) 140 °C; (ii) 420 °C; and (iii) target temperatures (i.e., T_{max}) of 670 °C or 725 °C for variable periods of time. These specific heating rates and constant temperature periods are identified in Table 1.

Table 1. Synthesis conditions for Ni-B compounds.

Run No.	Weight	Reactant Ni:B Ratio	T_{Max} (°C)	t_{M} (hours)	P_{Max} (MPa)	Compounds in Product
1	$\Sigma = 5.37$ g	1:2	725	5	1.9	Ni ₄ B ₃ (o; 88%) (Ni ₃ B)
2	$\Sigma = 5.37$ g	1:2	725	12	2.8	Ni ₄ B ₃ (o; 46%) Ni ₂ B (54%)
3	$\Sigma = 3.48$ g	4:3	670	5	3.4	Ni ₂ B (99%)
4	$\Sigma = 3.10$ g	2:1	670	5	2.3	Ni ₂ B (98%)
5	$\Sigma = 3.10$ g	2:1	670	40	2.5	Ni ₂ B (92%) Ni ₃ B (8%)
6	$\Sigma = 6.22$ g	2:1	670	5	4.9	Ni ₂ B (61%), Ni ₃ B (39%)
7	$\Sigma = 3.74$ g	3:1	670	5	2.2	Ni ₃ B (55%), Ni ₂ B (39%) Ni (6%)
8	$\Sigma = 3.74$ g	3:1	670	10	2.4	Ni ₃ B (72%), Ni ₂ B (17%) Ni (10%)
9	$\Sigma = 3.74$ g	3:1	670	15	2.3	Ni ₃ B (64%), Ni ₂ B (26%) Ni (10%)

2.2. Characterization

Polycrystalline samples are characterized using X-ray powder diffraction and electron microscopy equipped with microanalysis. X-ray powder diffraction patterns are obtained using Co and Cu $K\alpha 1$ radiation in Bragg Brentano geometry with 0.02° 2θ steps and a counting time of 10 s per step using PANalytical X-ray diffractometers (Almelo, The Netherlands). Diffraction patterns are refined and indexed using the software program Topas (Florence, KY, USA) [27]. X-ray diffraction patterns and electron microscopy indicate that many synthesized samples are multiphase with Ni₂B, Ni₃B, or Ni₄B₃ as a predominant phase. Samples with high proportions of Ni₂B or Ni₃B (i.e., >95%) are selected for additional data collection using a PANalytical X-ray diffractometer for subsequent Rietveld refinement using Topas. Schematic models of crystal structures shown in Figure 1 are compiled by the program VESTA [28].

A Zeiss SigmaTM Field Emission Gemini SEM (Carl Zeiss Pty Ltd., North Ryde, Australia) equipped with an Oxford Instruments SDD XMax 50 mm² detector (Abington, UK) is used for microscopy observations and energy dispersive spectroscopy (EDS) analysis. Samples are prepared for SEM/EDS by placing a thin layer of powder onto aluminum stubs with double sided carbon tape. In general, samples are not coated with a conductive coating to avoid analytical interference(s). Elemental analysis is carried out at an accelerating voltage of 15 kV at 8.5 mm working distance. Excessively charging samples are imaged at lower accelerating voltages of 5 kV or 10 kV.

Microstructural features were examined on polished samples using a field emission JEOL 7001SEM (JEOL (Australasia) Pty Ltd., French's Forest, Australia), with automated feature detection equipped with secondary electron (SE, JEOL (Australasia) Pty Ltd., French's Forest, Australia), Oxford Instruments SDD XMax 50 mm² detector (Abington, UK) and an electron back-scatter diffraction (EBSD) pattern analyzer and Channel 5 analysis software. Fine polished samples mounted in

conductive resin were selected for EBSD mapping using an accelerating voltage of 15 kV and step size of 0.5 μm .

Quantitative elemental analyses are performed using a JEOL JXA 8530F field emission electron microprobe analyzer (EPMA, JEOL (Australasia) Pty Ltd., French's Forest, Australia) equipped with five wavelength-dispersive spectrometers and using *Probe for EPMA* software [25]. For these analyses, powder samples are mixed with conductive resin and placed in a 30 mm diameter mold inside a hot mounting press. The sample mount is polished with a series of diamond pads and cloths to a mirror finish suited to electron microprobe analysis. Spot analyses on borides are performed using the following combined conditions: B $K\alpha$ X-ray intensities are measured at 7 kV accelerating voltage, followed immediately by intensity measurement of the Ni $K\alpha$ X-ray line at 15 kV accelerating voltage. A focused beam is utilized and the beam current maintained at 40 nA under both conditions. Details on data collection methods, analyzing crystals, standard materials, and data reduction for EPMA analyses are provided in Shahbazi et al. [25].

In this study, the combined analytical conditions described above were chosen to localize the lateral and vertical spatial resolution from characteristic X-rays [25]. The detection limits under these conditions are 0.16 wt % for B and 0.04 wt % for Ni. The average analytical error for boron for individual spot analyses is 8.7%. A statistical program is used to determine the envelope for production of characteristic X-rays using the EPMA under these operating conditions. The lateral and vertical spatial resolutions for excitation of the $K\alpha$ X-ray lines of B and Ni is $<1 \mu\text{m}$ as calculated using the CASINO Monte Carlo modeling program for electron trajectories [25]. DC magnetization measurements are performed using a Cryogenics Ltd. Mini cryogen-free 5 T system (London, UK). The magnetization field isothermal loops are determined within $\pm 5 \text{ T}$ at 100 K.

3. Results

Data presented in this study are a summary of more than thirty separate experiments across a range of temperature and pressure conditions, and with different amounts and ratios of starting materials. We present a selection of these experimental data to demonstrate the range of conditions under which Ni-B compounds may form.

3.1. Synthesis

Selected reactions that illustrate the temperature and pressure conditions for production of Ni_2B , Ni_3B and $\text{o-Ni}_4\text{B}_3$ are listed in Table 1. In general, these reactions provide higher yield of nickel borides and, in some cases, single phase formation of Ni_2B . In all reactions, the maximum pressure (P_{max}) increases to between 1.9 MPa and 4.9 MPa when the reactor is at the maximum temperature. As shown in Table 1, the value of P_{max} varies for each reaction and is dependent on a number of variables including the ratio and amount of starting materials within the reactor. In general, a higher proportion and amount of NaBH_4 in the reaction results in a higher P_{max} .

Figure 2a illustrates the typical heating profile used for Runs 3, 4, 6, and 7 and is the general format for all other reactions not listed in Table 1. The pressure profiles for some reactions listed in Table 1 are shown in Figure 2b. The maximum pressure achieved during a reaction depends on the quantity of reactants, in particular of NaBH_4 , used in the reactor [25]. For all reactions, pressure increases to a maximum value (P_{max}) ranging between 2.3 MPa and 4.9 MPa at 670 $^\circ\text{C}$. A rapid increase in pressure occurs as the thermocouple records a ramp from $\sim 140 \text{ }^\circ\text{C}$ to 425 $^\circ\text{C}$ and also from 425 $^\circ\text{C}$ to 670 $^\circ\text{C}$. The fluctuations in pressure profiles shown in Figure 2 are points in the reaction at which phase transformations are rapidly occurring as noted in earlier work [26,29]. Similar pressure profiles are observed for all other reactions listed in Table 1.

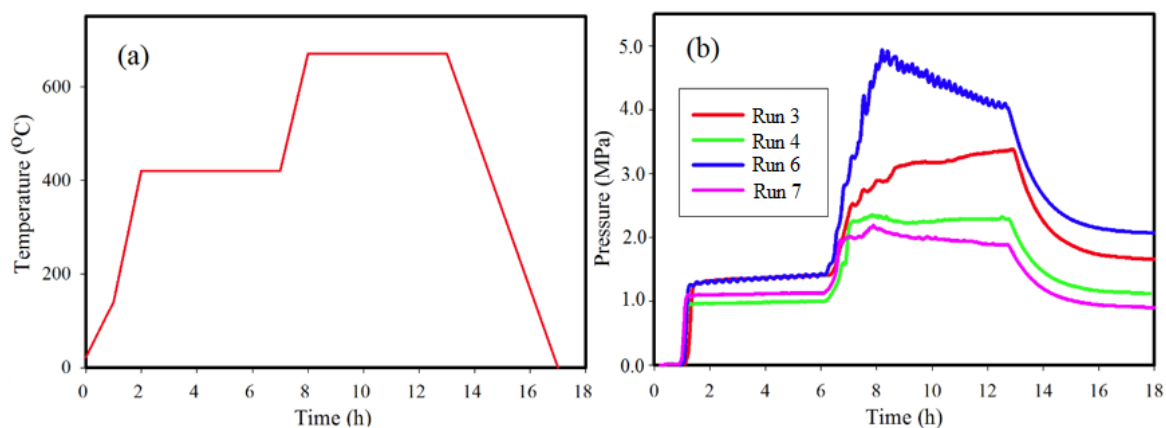


Figure 2. (a) Heating profile and (b) pressure profile for synthesis of Ni-B phases for Run 3, Run 4, Run 6, and Run 7 with conditions as listed in Table 1.

X-ray diffraction (XRD) and Rietveld refinements show that Ni_2B is the major phase for Run 3, Run 4, and Run 5 with maximum yields of 99%, 98%, and 92%, respectively (Table 1). XRD peaks corresponding to boron are not observed for Run 3 in which there is an excess of boron in the reactants compared with the stoichiometric product. This outcome may be due to a higher P_{max} compared with Run 4 and Run 5 or formation of gaseous phases that condense at the top of the reactor. However, an increased reaction time to 40 h at 670 °C (Run 5) shows a reduction in Ni_2B and a detectable quantity of Ni_3B .

A reaction at significantly higher P_{max} , as in Run 6 (Figure 2b and Table 1) achieved by increasing the amount of starting materials, results in substantially different proportions of Ni_2B and Ni_3B at 61% and 39%, respectively. The autogenous pressure for Run 6 is at a maximum of 4.9 MPa at T_{max} and may influence the formation of Ni_3B for starting compositions that are deficient in Ni. For stoichiometric amounts of starting materials (Runs 7 and 8; Table 1), a relatively minor increase in P_{max} also shows a higher Ni_3B yield albeit with residual Ni present. In comparison, Runs 8 and 9 show that with continued heating at 670 °C for a longer time, up to 15 h, the proportions of Ni_3B to Ni_2B shift in favor of increased Ni_2B production and decreased Ni_3B .

3.2. Structural Analysis

Powder diffraction patterns from selected samples listed in Table 1 are used for Rietveld refinement using Topas. Structural data from Kayser et al. and Havinga et al. [30,31] are used as input for refinement of XRD data for these samples. In the Ni-B system, peaks for Ni, $\text{o-Ni}_4\text{B}_3$, Ni_2B and Ni_3B are identified in XRD powder diffraction patterns. For reactions with more than one phase in the product, for example Run 5 (Table 1), refinements include allocation of diffraction peaks to each phase and unconstrained Rietveld refinement on all phases. As shown in Figure 3, Ni_2B and Ni_3B are readily distinguished using Rietveld refinement and visual inspection of peak intensities verifies that Ni_2B is the predominant phase. Table 2 shows refined lattice parameters for Ni_2B and Ni_3B for Run 4 and Run 8 from this study, respectively. The refined cell parameters are in good agreement with results from Kayser et al. and Havinga et al. [15,16] with good quality refinement parameters such as goodness-of-fit.

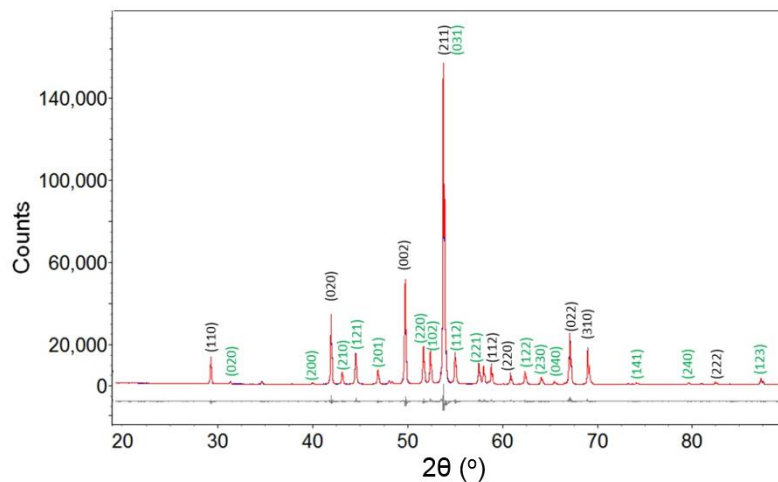


Figure 3. The experimental (blue), fitted (red) and difference (grey line below observed and calculated pattern) X-ray diffraction (XRD) profile for sample from Run 5. Indexed reflections for Ni_2B and Ni_3B are indexed with black and green color, respectively.

Table 2. Rietveld refinement data for Ni_2B and Ni_3B from Run 5 and Run 9.

Formula	Ni_3B (This Work)	Ni_3B [6]	Ni_2B (This Work)	Ni_2B [32]
Crystal System	Orthorhombic (Pnma)		Tetragonal (I4/mcm)	
a(Å)	5.2273 (1)	5.2195 (5)	4.9768 (1)	4.9910 (3)
b(Å)	6.6131 (1)	6.6164 (6)	4.9768 (1)	4.9910 (3)
c(Å)	4.3900 (1)	4.3912 (4)	4.2348 (0)	4.2470 (3)
Cell Vol. (Å ³)	151.756 (3)	151.65	104.891 (2)	105.79
R_{wp}	5.4		3.86	
R_{p}	3.86		2.61	
GoF	2.57		1.81	

3.3. Morphology and Microstructure

The morphology of Ni-B powders obtained from Run 3, Run 4, Run 6, and Run 8 are shown in Figure 4. The product is comprised of large aggregates with a broad distribution of many smaller particles. The Ni-B powders obtained at 670 °C are large aggregates consisting of well-defined, inter-penetrating polygonal particles with orthogonal morphology. In all samples produced by these syntheses, two different morphologies of aggregates are common; each of a size ranging from 2 μm up to 10 μm . These two morphologies are orthogonal or rectangular shaped and spherical shapes as shown in the insets of Figure 4c,d. Each aggregate morphology shows smooth surfaces with individual particles of size varying from 50 nm up to several hundred nm in size.

EBSD analyses of Ni-B aggregates from Run 3 and Run 8 are presented in Figure 5 without the use of noise reduction software applied to the maps. Figure 5a indicates Ni_2B is a major phase in the sample and confirms XRD data that ~99% of the Run 3 sample is Ni_2B . A very small region in Figure 5a shows also the presence of Ni_3B in green. Different microstructures were obtained for aggregates from Run 8, as illustrated in Figure 5c. According to the analysis using EBSD, three phases including Ni_2B , Ni_3B , and Ni are present in this sample. This determination is in good agreement with the XRD results for this sample (Table 1). Figure 5b,d clearly indicate that Ni_2B grains produced in Run 8 are significantly smaller than those produced in Run 3 due to different reaction conditions. An Euler map in Figure 5b suggests that small Ni_2B grains within the aggregate show a limited number of different orientations compared with the sample from Run 8 shown in Figure 5d. Texture maps can be used to evaluate grain orientation in these polished samples. For Run 3, these maps (not shown) show

that preferential grain orientation in these aggregates is along the [001] and [110] primary axes for Ni_2B grains.

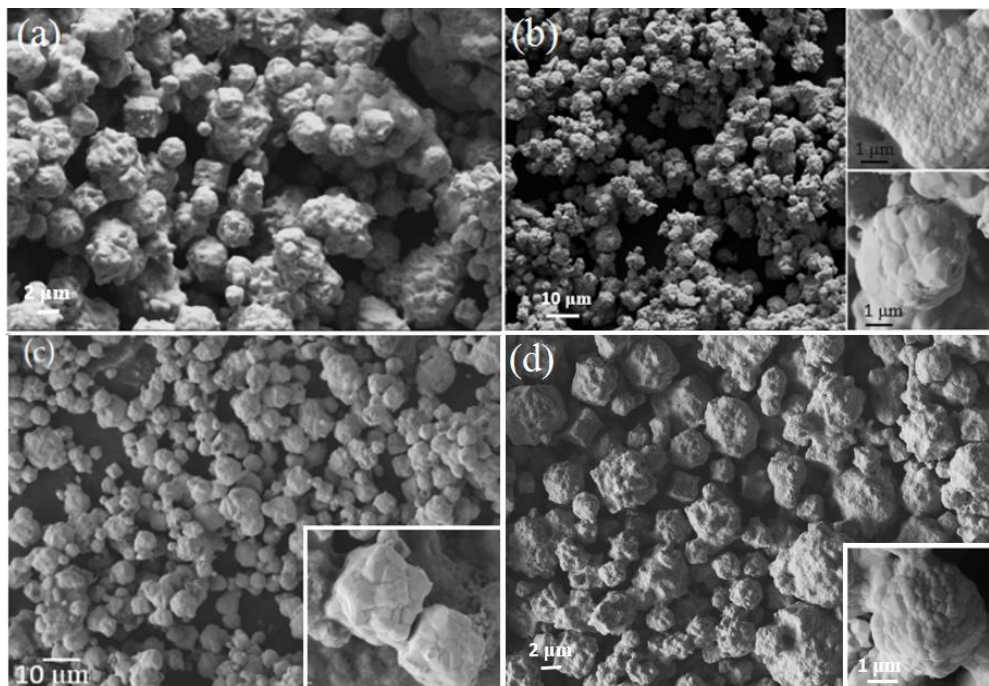


Figure 4. Scanning electron microscope (SEM) image of Ni-B powder from (a) Run 3, (b) Run 4, (c) Run 6, and (d) Run 8. Higher resolution SEM image shows (c) a cube and (d) sphere shaped morphology consisting of smoothly rounded crystals.

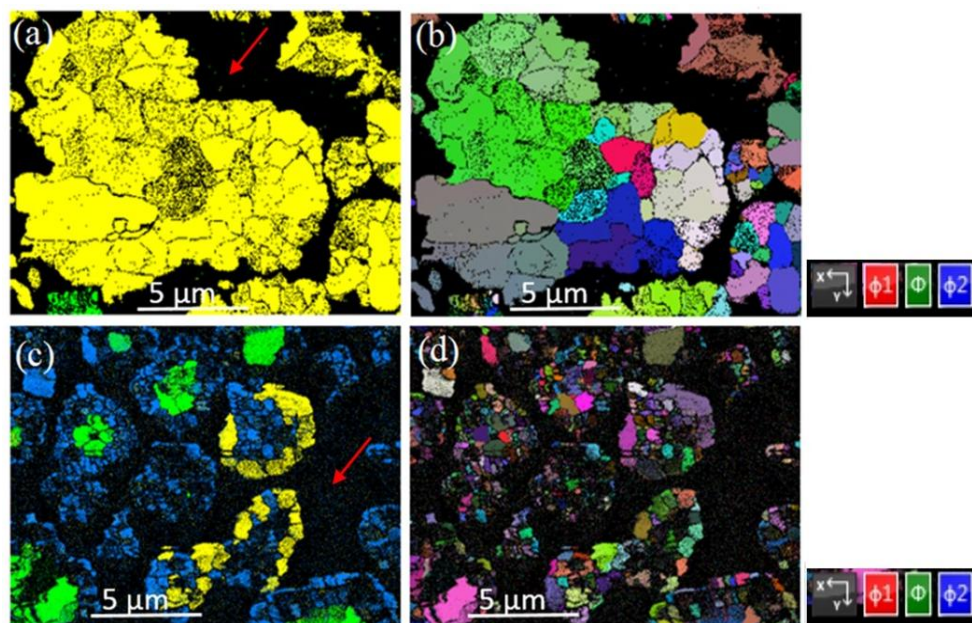


Figure 5. Electron back-scatter diffraction (EBSD) images of polished surfaces for Ni-B aggregates from Run 3 and Run 8. Red arrows indicate mounting resin. (a) EBSD map of the sample from Run 3 showing predominantly Ni_2B (yellow) with minor Ni_3B (green); (b) Euler map of the aggregate from Run 3 with polar orientations (right hand panel); (c) EBSD map of sample from Run 8 with three phases including Ni_2B (yellow), Ni_3B (blue) and Ni (green). (d) Euler map of the aggregates from Run 8.

Figure 6 uses the EBSD phase maps in Figure 5 to estimate the grain size distribution within an aggregate. For each analysis of Run 3 and Run 8 samples, approximately 300 grains are included in the dataset. The grain size distribution for Run 3 is substantially broader than that of aggregates in Run 8. Both graphs in Figure 6 show that the highest proportion of grains are sub-micron in size and that for Run 8 almost all grains are <1 μm .

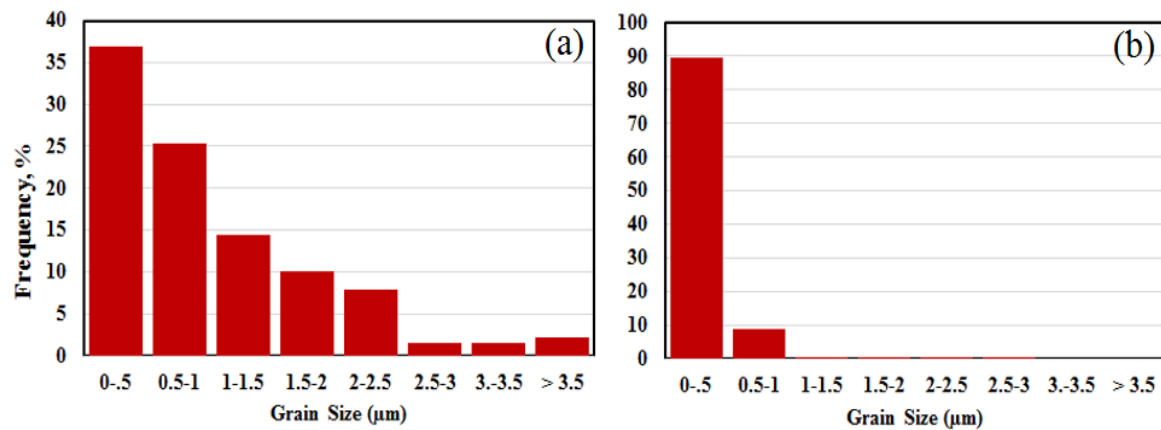


Figure 6. (a,b) Grain size distributions from Run 3 and Run 8, respectively, determined using EBSD data as shown in Figure 5.

Figure 7 shows backscattered electron images (BEIs) of aggregates from Run 3, Run 4, and Run 5. These images are used as a guide to identify locations for EPMA analyses and, in general, reflect differences in atomic number contrast within each aggregate. Table 3 provides average compositions from selected spot analyses of different aggregates from Runs 3–5. The number of point analyses used for average value determinations based on similar BEI contrast are listed in Table 3. Standard deviations are calculated on a basis of the number of analyses for each region within aggregates. These data show that the concentration of boron ranges between 0.52 wt % to 8.26 wt % and the concentration of nickel between 91.8 wt % and 99.3 wt % in the aggregates measured. As shown in Table 3, the stoichiometry of Ni-B phases include Ni_2B and Ni_3B in Run 3, Run 4, and Run 5. The stoichiometry in each case is based on an integer value for boron.

Table 3. Average compositions of selected regions in aggregates from Run 3, Run 4, and Run 5.

Compound	<i>n</i>	Element wt %			Stoichiometry		
		B	Ni	Totals	B	Ni	Totals
Run 3							
Ni_2B	7	8.1 (0.3)	92.4 (0.7)	100.5	1	2.1 (0.1)	3.1 (0.1)
$\text{Ni}_{2.2}\text{B}$	3	7.6	91.7 (0.3)	99.3 (0.3)	1	2.22 (0.02)	3.2 (0.02)
Ni_3B	2	5.4	94.3	99.8	1	3.20	4.2
Run 4							
Ni_2B	15	8.2 (0.2)	91.9 (0.3)	100.1 (0.4)	1	2.07(0.06)	3.1 (0.1)
Ni_3B	7	5.5 (0.3)	94.3 (0.5)	99.7 (0.3)	1	3.19(0.21)	4.2 (0.2)
$\text{Ni}_{3.5}\text{B}$	4	4.9 (0.1)	94.6 (0.2)	99.5 (0.2)	1	3.53 (0.09)	4.5 (0.1)
Run 5							
Ni_2B	12	8.3 (0.3)	92.2 (0.3)	100.5(0.5)	1	2.04(0.07)	3.0 (0.1)
Ni_3B	5	5.5 (0.1)	94.6 (0.4)	100.1 (0.4)	1	3.14(0.09)	4.1 (0.1)

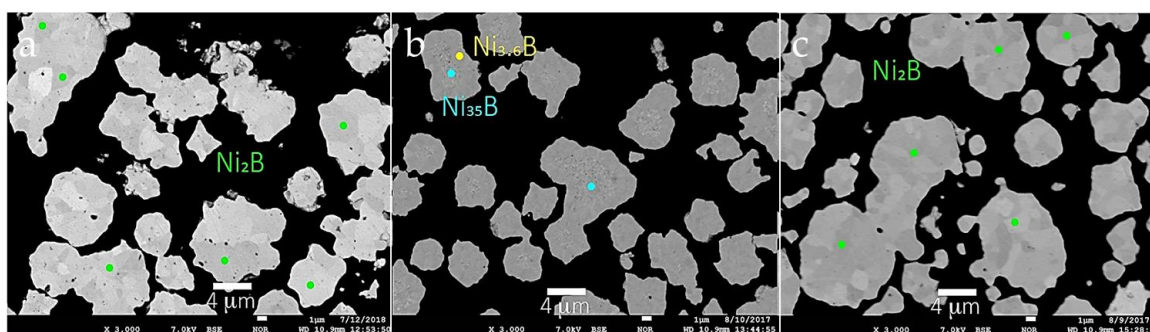


Figure 7. Backscattered electron images of aggregates from (a) Run 3; (b) Run 4; (c) Run 5. Colored circles denote locations of spot analyses using the EPMA coded to compositions listed in the figure.

However, for Run 4, a Ni-rich core and a Ni-B outer shell is observed and shown in Figure 7b. The inner region of this aggregate shows an average composition of $\text{Ni}_{35.1}\text{B}$, which was not observed by XRD. This composition may represent an unusual form of nickel boride, or alternatively, very fine-grained Ni metal particle(s) may be present in the core region of this grain. Detection of this Ni-rich region is due to the spatial and analytical resolution of the XRD vs. EPMA techniques. For example, XRD is a bulk technique that cannot detect phases present in amounts less than $\sim 5\%$. However, the detailed internal structures of individual particles that have a two-phase or multi-phase core-shell structure that evades detection by XRD are readily identified using BSE imaging at high magnification. Such core and shell compositions, respectively, can be analyzed by WDS on a field emission electron microprobe (FE-EPMA), which permits high precision micron to sub-micron scale quantitative analysis. The interface region of an aggregate in this sample shows an average composition of $\text{Ni}_{3.4}\text{B}$. These compositions are different to the stoichiometry of the starting materials.

EPMA analysis for aggregates from Run 3 with the Ni:B ratio of 4:3 shows an average composition of $\text{Ni}_{2.1}\text{B}$ and a fewer number of grains with $\text{Ni}_{3.20}\text{B}$ composition. This latter composition is in general agreement with observation of a minor Ni_3B phase using EBSD analysis (Figure 5a). However, peaks from Ni_3B were not observed in the XRD diffraction pattern from Run 3. The starting materials in Run 3 have excess boron compared with other reactions listed in Table 1. The stoichiometry for samples with $\text{Ni}_{2.22}\text{B}$ may be re-expressed as $\text{Ni}_{6.67}\text{B}_3$, which is similar to the phase Ni_7B_3 of hexagonal symmetry in space group $\text{P6}_3\text{mc}$ [3] However, XRD data does not support an hexagonal structure for this predominant product from Run 3. More importantly, XRD data and results from EBSD analysis show that Ni_2B is the predominant phase from Run 3.

3.4. Magnetic Properties

The magnetization as a function of the applied field is determined for products from Run 4 (Ni_2B -98%), Run 6 (Ni_2B -61%, Ni_3B -39%), and Run 8 (Ni_2B -17%, Ni_3B -72% and Ni-10%) at 100 K. As shown in Figure 8, the M-H curve for product from Run 4 with nearly single phase Ni_2B displays a hysteresis curve with low magnetization values along with an increase in magnetization at low magnetic fields. The sample then saturates at an applied field of 0.15 T (inset). The magnetization data for products from Run 8 reveal a hysteresis loop with a significant increase in M value along with saturation at 0.25 T. This behavior could be due to the presence of two magnetic components; i.e., a ferromagnetic component such as Ni that is easily saturated at low field and a paramagnetic component such as Ni_3B and/or Ni_2B compounds. This interpretation is in agreement with results from XRD, EBSD, and EPMA analyses presented in earlier sections.

EPMA results for the sample from Run 4 show that areas with a nickel rich core are present and are identified in Figure 7b. The inclusion of nickel-rich phases (such as $\text{Ni}_{35.1}\text{B}$ or Ni) may result in a minor hysteresis effect in magnetic measurements. Magnetic measurement of the product from Run 8 with a dominant Ni_3B phase and 10% Ni—as indicated by XRD results—reveals a larger hysteresis

loop due to the higher amount of Ni present. The lower value of magnetization for the product from Run 4 is consistent with the known weak paramagnetic behavior of Ni_2B [33]. The magnetization measurement for Run 6 displays low magnetization values along with an increase in magnetization at a low magnetic field and then saturation at an applied field of 0.2 T. Unlike the other two samples, hysteresis is not observed for this sample from Run 6. In this case, the absence of Ni or Ni-rich particles is consistent with the observed hysteresis behavior of the sample.

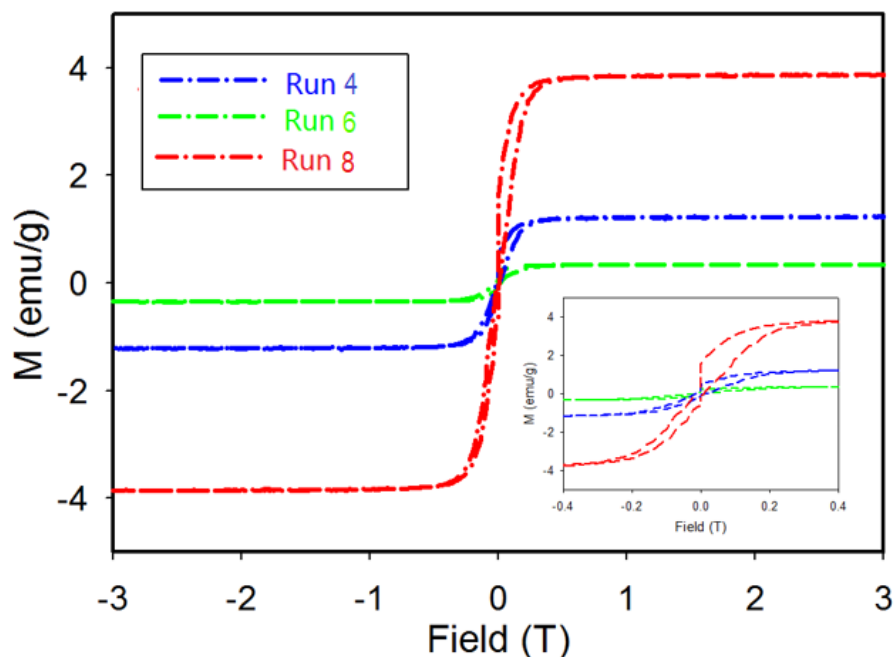


Figure 8. Field dependent magnetization at 100 K for samples from Run 4, Run 6, and Run 8. Inset: Detailed view of magnetization at low field.

4. Discussion

In general, syntheses of Ni-B compounds are based on (i) solid-state methods that include mechanical mixing of components followed by heating and sintering protocols under reducing conditions or (ii) solution based methods that involve precipitation of precursor components that are, preferably, intimately mixed at nano-scale followed by heating and sintering under reducing conditions. In the latter case, if the mixture of components is effective and intimate, then the achievement of a specific stoichiometric composition of Ni-B compound can be achieved at a lower temperature than solid-state methods.

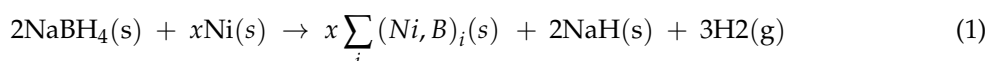
The production of metal borides via room temperature hydrolysis of NaBH_4 , sometimes catalyzed by a salt, is well known [21]. More recently, metal borides have been produced with organic compounds such as tetraethyleneglycol (TEG) [23] and tetrahydrofuran (THF) as solvent [15]. In these instances, it is critical to thoroughly wash the resultant precipitate, which may be crystalline [15] or amorphous [14] in order to remove remnant salts or solvents. These requirements and the potential for production of mixed phases [23] suggests that single step syntheses of a stoichiometric nickel boride by solution based methods are unlikely. Nevertheless, this polyol or modified polyol approach can result in the direct formation of nanocrystalline metal borides without a requirement for post-synthesis annealing [23].

In this work, we explore the potential for single step synthesis of crystalline nickel borides using the known reactivity of NaBH_4 on heating with specific metals. The capacity for NaBH_4 to generate gases (e.g., B_2H_6 and/or H_2) via pyrolysis in the presence of specific metals was identified in the 1950s [34]. We have exploited this characteristic of NaBH_4 and KBH_4 in order to form MgB_2 [26,29] and Mg-Ni borides [25] under similar reactor conditions. A consistent heating protocol is utilized for all

experiments albeit with variations in the hold time at maximum temperature of reaction. Autogenous pressure is moderated by the ratio of reactants (e.g., Ni to NaBH₄) and the volume of NaBH₄ in the starting mixture. As shown in Table 1, the ratio of reactants also influences the optimal stoichiometry of a final product.

4.1. Synthesis of Nickel Borides

Different nickel boride phases can be produced at moderate temperatures by heating Ni and NaBH₄ under autogenous pressure generated by the decomposition of the borohydride. The general chemical equation that describes this reaction is:

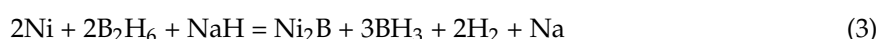


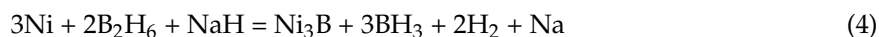
where (Ni, B)_i stands for any possible binary solid phase formed by Ni and B. In this generic case, different reaction paths may occur and the exact mass balance of a specific reaction will depend on the ratio of starting materials as well as the number of nickel boride phases formed and their resultant stoichiometry. According to (1) above, the maximum amount of gas produced from the decomposition of NaBH₄ is three moles of H₂ for every two moles of NaBH₄. In general, this trend is observed across the full range of experiments as well as those presented in Table 1. However, at the temperatures achieved in these experiments other hydrides, such as NaH, may also form as a gaseous species [26].

The optimum conditions for formation of Ni₂B using NaBH₄ and Ni metal are T_{max} = 670 °C and 2.3 MPa < P_{max} < 3.4 MPa with maximum yield of 98–99%, determined by XRD as shown in Table 1. Orthorhombic Ni₄B₃ forms at higher temperature (~725 °C) than Ni₂B under these conditions (i.e., 1.9 MPa < P_{max} < 2.8 MPa) with yield up to 88% and at a lower pressure. Our assumption that a longer hold time at 725 °C would reap a higher yield of o-Ni₄B₃ did not materialize despite a number of attempts (data not shown) and suggests that the phase diagram under these conditions is complex, particularly given the substantial presence of Ni₂B in Run 2 at pressures overlapping with those achieved in Runs 3 and 4.

Figure 2 shows the autogenous pressure changes with reaction for both Run 3 and Run 4. For both reactions, the autogenous pressure remains relatively constant during the hold at T_{max} (i.e., ~670 °C) unlike the pressure profile for Run 6. The higher pressure achieved in Run 3 compared to Run 4 is due to a higher amount and proportion of NaBH₄ in the reactant mix, yet allows an estimate of the boundary conditions for formation of Ni₂B. The profiles for Run 3 and Run 4 at T_{max} suggest that the optimum equilibrium conditions for formation of Ni₂B using autogenous pressure are achieved with a resultant high yield. The outcome from Run 5, which is a repeat of Run 4 but for a longer hold time (8x longer) at T_{max}, suggests that Ni₃B may be a preferred stable phase at this temperature and pressure.

In all cases shown in Figure 2, autogenous pressure increases rapidly as the reaction temperature increases to 420 °C. We have shown in previous work [25,26,29] that this rise in autogenous pressure is due to formation of H₂ and B₂H₆ by the decomposition of NaBH₄. This decomposition of NaBH₄ increases rapidly with temperatures above 400 °C and will depend on the relative proportions of reactants, pressure, temperature and heating rates. In Run 6 (Figure 2), the pressure is the highest of those listed due to the higher total amount of reactants and with proportionately more NaBH₄ than in other runs. The irregular changes in pressure and the significant drop in autogenous pressure (Δ~1 MPa) during the hold at T_{max} for Run 6 suggests that under these conditions, Ni₂B and Ni₃B are competing for the available resource—boron—to form a stable phase. As B₂H₆ is used in the reaction, H₂ remains and provides the ambient pressure once T ~25 °C at the end of the reaction. The competing reactions at T_{max} are (3) and (4) as shown below:





Reactions (3) and (4) are balanced equations for a closed system but the detail of processes occurring in these reactions is difficult to verify. As noted in earlier work [26], the decomposition of NaBH_4 may occur at low temperatures ($<200\text{ }^\circ\text{C}$) in the presence of a metal catalyst [29] and accelerates at temperatures above $\sim 400\text{ }^\circ\text{C}$ *via* formation of lattice defects resulting in the production of BH_3 and NaH [35]. We surmise that formation of BH_3 gas which readily polymerizes to form B_2H_6 and higher forms [36] is promoted under the conditions inherent in the reactor. In addition, the melting point for NaH is $300\text{ }^\circ\text{C}$ and the melting point for NaBH_4 is $505\text{ }^\circ\text{C}$ at standard pressure [37]. However, the melting point for NaBH_4 is shown to decrease in the presence of metals [38,39] but may increase to $535\text{ }^\circ\text{C}$ under 0.1 MPa hydrogen pressure [38]. Other factors that influence the intermediate reactions between $\sim 400\text{ }^\circ\text{C}$ and $675\text{ }^\circ\text{C}$ include the formation of liquid Na and the rapid increase in vapour pressure of Na to 0.089 kPa above $420\text{ }^\circ\text{C}$ at 0.1 MPa [40]. Hence, we offer reactions (3) and (4) above as possible pathways for the formation of Ni_2B and Ni_3B under these reactor conditions.

The data for Runs 7 and 8, when compared with Run 6, show that a higher proportion of Ni in the reaction mix results in a shift in the equilibrium between Ni_2B and Ni_3B at lower autogenous pressure (i.e., $\sim 2.2\text{ MPa}$). In addition, a longer hold time at $\sim 670\text{ }^\circ\text{C}$ results in a higher relative yield of Ni_3B . In both cases, excess Ni is present in the reactants which we presume to be at the expense of Ni_2B formation. As shown in Run 9, a longer hold time at $\sim 670\text{ }^\circ\text{C}$ for up to 15 h shifts the reaction back in favour of Ni_2B , and outlines the limits of the phase field for formation of Ni_2B and Ni_3B under these conditions.

X-ray diffraction experiments by Kapfenberger et al. [14] under ambient atmosphere conditions indicate that crystalline Ni_3B forms at about $320\text{ }^\circ\text{C}$. Other syntheses, such as the modified polyol process using TEG or mechanical alloying also indicate that Ni_3B forms at lower temperatures than Ni_2B . For example, the lowest temperature for Ni_3B formation using a TEG polyol process is $\sim 265\text{ }^\circ\text{C}$ but above $400\text{ }^\circ\text{C}$ Ni also forms in the product [23]. Similarly, with mechanical alloying Ni_3B forms at a lower temperature ($\sim 350\text{ }^\circ\text{C}$) than Ni_2B ($\sim 700\text{ }^\circ\text{C}$) [41]. While these synthesis methods are not directly comparable, we surmise that formation of Ni_3B at lower temperatures than Ni_2B from a given starting composition is consistent with the data presented in this work using autogenous pressure pyrolysis.

Ni_2B is stable up to high pressures at ambient temperature [42] but is less amenable to solvo-thermal methods of synthesis. Feng et al. [20] produced Ni_2B at $\sim 420\text{ }^\circ\text{C}$ with 60% yield using benzene as the solvent. Other methods, such as with an RF thermal plasma produce Ni_2B from Ni and B precursors but in a multi-phase mix with Ni_3B and Ni_4B_3 . The highest yield of Ni_2B by this process is $\sim 28\%$ [43]. Conventional solid state methods to synthesize Ni_2B using Ni and B powders heated to temperatures $>850\text{ }^\circ\text{C}$ in an enclosed capsule [17] is a well utilised approach to obtain single phase product. In comparison, the use of autogenous pressure generated by heating NaBH_4 in the presence of Ni powder generates predominantly single phase Ni_2B at lower temperature as shown by powder XRD in Table 1. The presence of minor quantities of other phases such as Ni_3B (see Table 3) is only detectable *via* more spatially precise methods such as EPMA. We propose that phase pure (i.e., 100% yield) Ni_2B using this method can be achieved by fine-tuning experimental parameters such as the ratio of reactants, the reaction temperature profile and T_{max} .

4.2. Magnetic Properties

The magnetic properties of transition metal metalloid crystalline compounds are very similar to amorphous counterparts with the same composition [1,7,8,10,44]. Gelatt et al. [45] report that the magnetic properties of the Ni-B system are governed by both B p orbitals and Ni d orbital– B p orbital interaction [45]. The B-B zigzag chains expand through NiB structures with increased B content. As the Ni content is diluted by boron, the Ni d orbital bonding becomes weaker. However, d states interact with metalloid s and p states, forming bonding and antibonding hybrids which can be more effective in bonding than the parent states. These bonding mechanisms strongly affect the formation of ferromagnetic states [46].

The M-H curve for the product from Run 4 with very high yield of Ni₂B displays a hysteresis curve with low magnetization values along with an increase in magnetization at low magnetic fields. As shown in Figure 8, the magnetization saturates at an applied field of 0.15 T (inset). On the other hand, the product(s) from Run 8, with high Ni₃B content shows a hysteresis loop with a significant increase in M value and saturation at 0.25 T (Figure 8). This behaviour is due to the presence of a ferromagnetic component (e.g., Ni) that easily saturates at low field and the presence of paramagnetic components such as Ni₃B and Ni₂B. As shown in Figure 5c, the product from Run 8 contains Ni particles embedded in paramagnetic Ni₃B and Ni₂B matrixes.

Thus, in general, our results from XRD, EBSD and EPMA analyses are consistent with high sensitivity magnetic measurements of these samples. While it is uncommon to present data on mixed phase materials, the magnetic properties shown in Figure 8 demonstrate that low levels of ferromagnetic material(s) can also be reliably detected by this technique. The higher magnetization value and broader hysteresis loop for the sample from Run 8, compared with Run 4 and Run 6 shown in Figure 8, is due to the higher Ni content as confirmed by XRD Rietveld analysis. The lower values of magnetization for products from Run 4 and Run 6 are also consistent with the weak paramagnetic behaviour of Ni₂B [33,46] and the relative proportions determined by XRD. The absence of Ni in Run 6 product is also consistent with an absence of hysteresis in the data shown in Figure 8.

5. Conclusions

Crystalline Ni₂B, Ni₃B and o-Ni₃B₄ compounds have been synthesised at moderate temperature and autogenous pressure using a single step process. These syntheses utilise autogenous pressure derived from the decomposition of sodium borohydride in the presence of Ni. The optimum pressure attained *via* this process for high yield Ni₂B synthesis is ~2.3–3.4 MPa at a maximum temperature of ~670 °C. The molar ratio of sodium borohydride to nickel powder affects not only the granularity and crystallinity of boride products but also the final composition. Spatially and chemically precise EPMA analyses show that boron content ranges from 0.5 to 8.5 wt % and nickel content from 91.7 to 99.3 wt % in the samples measured. This autogenous pressure method produces Ni₂B in high yield and at lower temperatures than solid state methods.

Author Contributions: Conceptualization, I.M. and M.S.; Methodology, M.S., H.C., N.D. and I.M.; Software, H.C. and M.S.; Formal Analysis, M.S. and H.C.; Investigation, I.M. and M.S.; Data Curation, M.S., H.C. and N.D.; Writing—Original Draft Preparation, M.S.; Writing—Review & Editing, I.M. and M.S.; Visualization, M.S., I.M., H.C. and N.D.; Supervision, I.M.

Funding: This research received no external funding.

Acknowledgments: This research received no external funding from agencies in the public, commercial or not-for-profit sectors. Access to, and ongoing assistance from, QUT's Central Analytical Research Facility (CARF) administered by the Institute for Future Environments is gratefully acknowledged. In particular, advice on sample preparation techniques and support from Don McAuley are especially appreciated.

Conflicts of Interest: The authors declare no conflict of interest.

References

1. Fruchart, R.; Roger, A.; Senateur, J.P. Crystallographic and Magnetic Properties of Solid Solutions of the Phosphides M₂P, M = Cr, Mn, Fe, Co, and Ni. *J. Appl. Phys.* **1969**, *40*, 1250–1257. [[CrossRef](#)]
2. Gumenuik, R.; Borrmann, H.; Leithe-Jasper, A. Refinement of the crystal structures of trinickel boron, Ni₃B, and tripalladium boron, Pd₃B. *Z. Kristallogr. New Cryst. Struct.* **2006**, *221*, 425–426. [[CrossRef](#)]
3. Hofmann, K.; Kalyon, N.; Kapfenberger, C.; Lamontagne, L.; Zarrini, S.; Berger, R.; Seshadri, R.; Albert, B. Metastable Ni₇B₃: A New Paramagnetic Boride from Solution Chemistry, Its Crystal Structure and Magnetic Properties. *Inorg. Chem.* **2015**, *54*, 10873–10877. [[CrossRef](#)] [[PubMed](#)]
4. Rundqvist, S. Crystal Structure of Ni₃B and Co₃B. *Acta Chem. Scand.* **1958**, *12*, 658–662. [[CrossRef](#)]
5. Rundqvist, S. An X-ray Investigation of the Nickel-Boron System. The Crystal Structures of Orthorhombic and Monoclinic Ni₄B₃. *Acta Chem. Scand.* **1958**, *12*, 1193–1208. [[CrossRef](#)]

6. Rundqvist, S.; Pramatus, S. Crystal Structure Refinements of Ni₃B, o-Ni₄B₃, and m-Ni₄B₃. *Acta Chem. Scand.* **1967**, *21*, 191–194. [[CrossRef](#)]
7. Bakonyi, I.; Babić, E.; Miljak, M.; Lück, R.; Bahle, J.; Hasegawa, R.; Kollár, J. Magnetic properties of amorphous, crystalline, and liquid Ni-B alloys. *Phys. Rev. B* **2002**, *65*, 104423. [[CrossRef](#)]
8. Bakonyi, I.; Panissod, P.; Hasegawa, R. Magnetic properties of a glassy Ni_{81.5}B_{18.5} alloy. *J. Appl. Phys.* **1982**, *53*, 7771–7773. [[CrossRef](#)]
9. Rojo, J.M.; Hernando, A.; El Ghannami, M.; García-Escorial, A.; González, M.A.; García-Martínez, R.; Ricciarelli, L. Observation and Characterization of Ferromagnetic Amorphous Nickel. *Phys. Rev. Lett.* **1996**, *76*, 4833–4836. [[CrossRef](#)] [[PubMed](#)]
10. Singh, V.; Banerjee, P.; Srinivas, V.; Babu, N.H.; Ghoshray, A.; Bandyopadhyay, B.; Mazumdar, C. Structural and Magnetic Properties of Ni Rich Amorphous Boride Nanoparticles. *AIP Conf. Proc.* **2011**, 256–259. [[CrossRef](#)]
11. Wade, R.C.; Holah, D.G.; Hughes, A.N.; Hui, B.C. Catalytically Active Borohydride-Reduced Nickel and Cobalt Systems. *Catal. Rev.* **1976**, *14*, 211–246. [[CrossRef](#)]
12. Jiang, Z.; Yang, H.; Wei, Z.; Xie, Z.; Zhong, W.; Wei, S. Catalytic properties and structures of nano-amorphous Ni-B alloys affected by annealing temperatures. *Appl. Catal. A* **2005**, *279*, 165–171. [[CrossRef](#)]
13. Wu, Z.; Mao, X.; Zi, Q.; Zhang, R.; Dou, T.; Yip, A.C.K. Mechanism and kinetics of sodium borohydride hydrolysis over crystalline nickel and nickel boride and amorphous nickel–boron nanoparticles. *J. Power Sources* **2014**, *268*, 596–603. [[CrossRef](#)]
14. Kapfenberger, C.; Hofmann, K.; Albert, B. Room-temperature synthesis of metal borides. *Solid State Sci.* **2003**, *5*, 925–930. [[CrossRef](#)]
15. Caputo, R.; Guzzetta, F.; Angerhofer, A. Room-temperature synthesis of nickel borides via decomposition of NaBH₄ promoted by nickel bromide. *Inorg. Chem.* **2010**, *49*, 8756–8762. [[CrossRef](#)] [[PubMed](#)]
16. Jiang, W.J.; Niu, S.; Tang, T.; Zhang, Q.H.; Liu, X.Z.; Zhang, Y.; Chen, Y.Y.; Li, J.H.; Gu, L.; Wan, L.J.; et al. Crystallinity-Modulated Electrocatalytic Activity of a Nickel(II) Borate Thin Layer on Ni₃B for Efficient Water Oxidation. *Angew. Chem. Int. Ed. Engl.* **2017**, *56*, 6572–6577. [[CrossRef](#)] [[PubMed](#)]
17. Kiessling, R. The Borides of Some Transition Elements. *Acta Chem. Scand.* **1950**, *4*, 209–227. [[CrossRef](#)]
18. Corrias, A.; Ennas, G.; Marongiu, G.; Musinu, A.; Paschina, G.; Zedda, D. The synthesis of nanocrystalline nickel boride powders by ball milling of elemental components. *Mater. Sci. Eng. A* **1995**, *204*, 211–216. [[CrossRef](#)]
19. Özbek, I.; Akbulut, H.; Zeytin, S.; Bindal, C.; Ucisik, A.H. The characterization of borided 99.5% purity nickel. *Surf. Coat. Technol.* **2000**, *126*, 166–170. [[CrossRef](#)]
20. Feng, X.; Bai, Y.; Lü, B.; Zhao, Y.; Yang, J.; Chi, J. Synthesis of nanocrystalline Ni₂B via a solvo-thermal route. *Inorg. Chem. Commun.* **2004**, *7*, 189–191. [[CrossRef](#)]
21. Schlesinger, H.I.; Brown, H.C.; Finholt, A.E.; Gilbreath, J.R.; Hoekstra, H.R.; Hyde, E.K. Sodium Borohydride, Its Hydrolysis and its Use as a Reducing Agent and in the Generation of Hydrogen. *J. Am. Chem. Soc.* **1953**, *75*, 215–219. [[CrossRef](#)]
22. Li, H.; Li, H.; Deng, J.-F. The crystallization process of ultrafine Ni-B amorphous alloy. *Mater. Lett.* **2001**, *50*, 41–46. [[CrossRef](#)]
23. Schaefer, Z.L.; Ke, X.; Schiffer, P.; Schaak, R.E. Direct Solution Synthesis, Reaction Pathway Studies, and Structural Characterization of Crystalline Ni₃B Nanoparticles. *J. Phys. Chem. C* **2008**, *112*, 19846–19851. [[CrossRef](#)]
24. Molvinger, K.; Lopez, M.; Court, J. Asymmetric reduction and hydrogenation over heterogenous catalysts prepared by reacting nickel-boride with norephedrine. *J. Mol. Catal. A Chem.* **1999**, *150*, 267–273. [[CrossRef](#)]
25. Shahbazi, M.; Cathey, H.; Mackinnon, I.D.R. Synthesis of Magnesium Nickel Boride Aggregates via Borohydride Autogenous Pressure. *Materials* **2018**, *11*, 480. [[CrossRef](#)] [[PubMed](#)]
26. Mackinnon, I.D.R.; Winnett, A.; Alarco, J.; Talbot, P. Synthesis of MgB₂ at Low Temperature and Autogenous Pressure. *Materials* **2014**, *7*, 3901–3918. [[CrossRef](#)] [[PubMed](#)]
27. McCusker, L.B.; Von Dreele, R.B.; Cox, D.E.; Louër, D.; Scardi, P. Rietveld refinement guidelines. *J. Appl. Crystallogr.* **1999**, *32*, 36–50. [[CrossRef](#)]
28. Momma, K.; Izumi, F. VESTA 3 for three-dimensional visualization of crystal, volumetric and morphology data. *J. Appl. Cryst.* **2011**, *44*, 1272–1276. [[CrossRef](#)]

29. Mackinnon, I.D.R.; Shahbazi, M.; Alarco, J.A.; Talbot, P.C. Low temperature decomposition of metal borohydride drives autogenous synthesis of MgB_2 . *Supercond. Sci. Technol.* **2017**, *30*, 055004. [[CrossRef](#)]
30. Kayser, G.F.; Kayser, F.X. Ni₃B: Powder diffraction pattern and lattice parameters. *J. Alloys Compd.* **1996**, *233*, 74–79. [[CrossRef](#)]
31. Havinga, E.E.; Damsma, H.; Hokkeling, P. Compounds and pseudo-binary alloys with the CuAl₂(C16)-type structure I. Preparation and X-ray results. *J. Less Common Met.* **1972**, *27*, 169–186. [[CrossRef](#)]
32. Villars, P.; Cenzual, K. *Pearson's Crystal Data CD-ROM*; AMS International: Materials Park, OH, USA, 2011.
33. Stahl, B.; Gajbhiye, N.S.; Wilde, G.; Kramer, D.; Ellrich, J.; Ghafari, M.; Hahn, H.; Gleiter, H.; Weimller, J.; Wrschum, R.; et al. Electronic and Magnetic Properties of Monodispersed FePt Nanoparticles. *Adv. Mater.* **2002**, *14*, 24–27. [[CrossRef](#)]
34. Bragg, J.K.; McCarty, L.V.; Norton, F.J. Kinetics of Pyrolysis of Diborane. *J. Am. Chem. Soc.* **1951**, *73*, 2134–2140. [[CrossRef](#)]
35. Cakir, D.; de Wijs, G.A.; Brocks, G. Native Defects and the Dehydrogenation of NaBH₄. *J. Phys. Chem. C* **2011**, *115*, 24429–24434. [[CrossRef](#)]
36. Czujko, T.; Varin, R.A.; Wronski, Z.; Zaranski, Z.; Durejko, T. Synthesis and hydrogen desorption properties of nanocomposite magnesium hydride with sodium borohydride (MgH₂ + NaBH₄). *J. Alloys Compd.* **2007**, *427*, 291–299. [[CrossRef](#)]
37. Orimo, S.; Nakamori, Y.; Eliseo, J.R.; Zuttel, A.; Jensen, C.M. Complex Hydrides for Hydrogen Storage. *Chem. Rev.* **2007**, *107*, 4111–4132. [[CrossRef](#)] [[PubMed](#)]
38. Martelli, P.; Caputo, R.; Remhof, A.; Mauron, P.; Borgschulte, A.; Zttel, A. Stability and Decomposition of NaBH₄. *J. Phys. Chem. C* **2010**, *114*, 7173–7177. [[CrossRef](#)]
39. Varin, R.A.; Czujko, T.; Wronski, Z.S. *Nanomaterials for Solid State Hydrogen Storage*; Springer: New York, NY, USA, 2009.
40. Haynes, W.M. *CRC Handbook of Chemistry and Physics*; CRC Press: Boca Raton, FL, USA, 2014.
41. Nazarian-Samani, M.; Kamali, A.R.; Mobarra, R.; Nazarian-Samani, M. Phase transformations of Ni-15 wt.% B powders during mechanical alloying and annealing. *Mater. Lett.* **2010**, *64*, 309–312. [[CrossRef](#)]
42. Chandra Shekar, N.V.; Sekar, M.; Sahu, P.C. Equation of state and compressibility of nickel semiboride. *Phys. B Condens. Matter* **2014**, *443*, 95–98. [[CrossRef](#)]
43. Cheng, Y.; Tanaka, M.; Watanabe, T.; Choi, S.Y.; Shin, M.S.; Lee, K.H. Synthesis of Ni₂B nanoparticles by RF thermal plasma for fuel cell catalyst. *J. Phys. Conf. Ser.* **2014**, *518*, 012026. [[CrossRef](#)]
44. Singh, V.; Srinivas, V. Evolution of Ni:B₂O₃ core-shell structure and magnetic properties on devitrification of amorphous NiB particles in air. *J. Appl. Phys.* **2009**, *106*, 053910. [[CrossRef](#)]
45. Gelatt, C.D.; Williams, A.R.; Moruzzi, V.L. Theory of bonding of transition metals to nontransition metals. *Phys. Rev. B* **1983**, *27*, 2005–2013. [[CrossRef](#)]
46. Bratkovsky, A.M.; Rashkeev, S.N.; Wendin, G. Electronic structure, ferromagnetism, and EELS spectra of crystalline alloys Fe_nB and Ni_nB (*n* = 1, 2, 3): Aspects of universal behavior. *Phys. Rev. B* **1993**, *48*, 6260–6270. [[CrossRef](#)]

